Post-Print

This is the accepted version of:

J. Huang, J.D. Biggs, N. Cui
Families of Halo Orbits in the Elliptic Restricted Three-Body Problem for a Solar Sail with Reflectivity Control Devices
Advances in Space Research, Vol. 65, N. 3, 2020, p. 1070-1082
doi:10.1016/j.asr.2019.10.010

The final publication is available at https://doi.org/10.1016/j.asr.2019.10.010

Access to the published version may require subscription.

Families of halo orbits in the elliptic restricted three-body problem for a solar sail with reflectivity control devices

Jia Huang[a,b,*], James D. Biggs[c], Naigang Cui[a]

[a] *School of Astronautics, Harbin Institute of Technology, Harbin 150001, China*
[b] *Institute of Systems Engineering, China Academy of Engineering Physics, Mianyang 621999, China*
[c] *Department of Aerospace Science and Technology, Politecnico di Milano, Milano 20156, Italy*

Abstract

Solar sail halo orbits designed in the Sun-Earth circular restricted three-body problem (CR3BP) provide inefficient reference orbits for station-keeping since the disturbance due to the eccentricity of the Earth's orbit has to be compensated for. This paper presents a strategy to compute families of halo orbits around the collinear artificial equilibrium points in the Sun-Earth elliptic restricted three-body problem (ER3BP) for a solar sail with reflectivity control devices (RCDs). In this non-autonomous model, periodic halo orbits only exist when their periods are equal to integer multiples of one year. Here multi-revolution halo orbits with periods equal to integer multiples of one year are constructed in the CR3BP and then used as seeds to numerically continue the halo orbits in the ER3BP. The linear stability of the orbits is analyzed which shows that the in-plane motion is unstable while the out-of-plane motion is neutrally stable and a bifurcation is identified. Finally, station-keeping is performed which shows that a reference orbit designed in the ER3BP is significantly more efficient than that designed in the CR3BP, while the addition of RCDs improve station-keeping performance and robustness to uncertainty in the sail lightness number.

*Corresponding author
Email address: caep_huangjia@163.com (Jia Huang)

Keywords: ER3BP, Halo orbit, Solar sail, Reflectivity control device, Station-keeping, 3rd order approximation

1. Introduction

Halo orbits around the collinear equilibrium points are widely used in deep-space missions due to their unique position for space weather observation and communication with the Earth. Halo orbits around the equilibrium point L_1 of the Sun-Earth system are used for observing the solar wind or for global Earth observation of the Sun-lit side, for example, ISEE-3, SOHO, WIND, Genesis and LISA Pathfinder (Shirobokov et al., 2017). Halo orbits around the equilibrium point L_2 of the Sun-Earth system are useful for space-based observatories, such as Herschel (ESA/NASA). Halo orbits around the equilibrium points L_2 of the Earth-Moon system can be used for observing the meteoroid impacts, such as LUMIO (ESA) (Cipriano et al., 2018).

Station-keeping on halo orbits has utilized chemical propellant to generate propulsion which limits the life-time of the mission. New types of propulsion systems such as solar sail propulsion use solar radiation pressure (SRP) to generate continuous and unlimited propulsion, which could significantly extend the life-time of deep-space missions. In addition, solar sails can enable an infinite number of artificial equilibrium points (AEPs) which are displaced from the traditional Lagrange points, as well as artificial halo orbits (AHOs) around these AEPs. Solar sails also enable the trajectories with reversal orbital angular momentum, called "H-reversal trajectories" (Zeng et al., 2019). These orbits have significant potential to extend the range of applications beyond that of traditional spacecraft (Gong and Macdonald, 2019). The design and computation of AHOs in the circular restricted three-body problem (CR3BP) and their applications have been addressed widely (Richardson, 1980a,c; Baoyin and Mcinnes, 2006; McInnes, 2000; Farrés and Jorba, 2010; Verrier et al., 2014; Heiligers et al., 2016; Waters and McInnes, 2007; Yuan et al., 2018; Dei Tos and Topputo, 2017). However, these orbits, despite giving insight into mission design of solar sails

applications, are not suitable for use as reference orbits for station-keeping as the disturbance due to eccentricity of the primaries orbits has to be compensated for. The eccentricity is the most significant perturbation in the Sun-Earth CR3BP (Richardson, 1980b). Moreover, a solar sail can only produce a small force and the attitude variation rates are slow. This limits their station-keeping capability and it is necessary to design reference orbits in higher-fidelity models.

In order to incorporate the effect of eccentricity and to design efficient station-keeping reference orbits, the solar sail elliptic restricted three-body problem (SSER3BP) should be considered. However, the challenge here is that the equations of motion of the elliptic restricted three-body problem (ER3BP) are non-autonomous since the true anomaly f varies with time. Therefore, periodic orbits in the Sun-Earth ER3BP only exist when their periods are equal to integer multiples of one year (Broucke, 1969). Periodic orbits in the classic ER3BP were investigated by Broucke (1969),Campagnola et al. (2008) and Hou and Liu (2011). In these papers, only isolated periodic orbits exist due to the constraint on the period, which prevents the numerical continuation of halo orbits with varying period. However, by utilizing SRP it is possible to obtain families of periodic orbit in the SSER3BP with fixed periods by varying the lightness number of solar sail.

Gong and Li (2015b) generated the out-of-plane periodic orbits in the SSER3BP by adjusting the sail angles together with the out-of-plane position to satisfy the equilibrium equations. Biggs et al. (2008, 2009) and Farrés and Jorba (2011) investigated one-year periodic orbits in the SSER3BP. Biggs et al. (2008, 2009) computed a one-year out-of-plane orbit in the solar sail CR3BP (SSCR3BP) and used this as a seed to numerically continue periodic orbits in the SSER3BP. Farrés and Jorba (2011) viewed the AEP in the SSCR3BP as a one-year periodic orbit in the inertial frame, which was used as a seed to generate families of periodic orbits in the SSER3BP using numerical continuation. However, solar sail AHOs around the collinear AEPs in the SSER3BP have not been investigated. In this paper, a strategy to generate families of AHOs around the collinear AEPs in the Sun-Earth SSER3BP is proposed. This approach is dif-

ferent from those discussed by Biggs et al. (2008, 2009) and Farrés and Jorba (2011) in which the one-year orbits in the SSCR3BP are used as seeds in a numerical continuation scheme. In this paper a wider class of AHOs with periods equal to fractions of one year are used as seeds and then numerically continued to yield multi-revolution AHOs whose periods equal integer multiples of one year. These AHOs are denoted as multi-revolution AHOs, as they wind around multiple times before coming back to exactly the same position. These multi-revolution AHOs are natural solutions to the SSER3BP and provide efficient reference orbits for station-keeping.

In this paper, reflectivity control devices (RCDs) are also used to control the magnitude of SRP of the sail without changing its attitude. This technology has been demonstrated as an attitude control actuation system for JAXA's small solar power sail demonstrator "IKAROS" (Funase et al., 2011). RCDs can switch the reflection properties from one state to another state. Two reflectivity modulation modes are possible, (i) the diffusion mode and (ii) the absorption mode. The diffusion mode can switch between specular reflection and diffusion, as demonstrated on "IKAROS" (Funase et al., 2011). The absorption mode switches between specular reflection and absorption. Aliasi et al. (2013) stabilized the AEPs using an absorption mode RCD solar sail with a fixed attitude. Gong and Li (2015a) investigated the equilibria in a Sun-asteroid system also using the absorption mode RCD solar sail. Lou et al. (2016) proposed an active disturbance rejection station-keeping control about equilibrium point orbits for an RCD solar sail using the same model as Gong and Li (2015a). Yuan et al. (2018) presented the families of Lyapunov and halo orbits in the SSCR3BP for an RCD solar sail. Coupled orbit and attitude control approaches for RCD solar sails were proposed by Mu et al. (2015) and Biggs and Negri (2019). RCDs have also been proposed to obtain the smart dust trajectory control in a heliocentric mission scenario (Mengali and Quarta, 2016; Mengali et al., 2018; Niccolai et al., 2019). In this paper, a more general and realistic model of the diffusion mode RCD solar sail is used which considers specular reflection, absorption, diffusion, and emission.

The linear stability of the orbits is analyzed, showing that the in-plane motion is unstable while the out-of-plane motion is neutrally stable and a bifurcation is identified. Station-keeping is then undertaken for a normal solar sail and for an RCD solar sail based on an application of LQR control. The reference orbits are chosen from the generated families of multi-revolution AHOs. Simulations are undertaken to compare and analyze the station-keeping performances. The results show that a reference orbit designed in the SSER3BP is significantly more efficient for station-keeping than a reference orbit designed in the SSCR3BP. In addition, the inclusion of RCD technology is shown to improve the station-keeping performance and provide additional robustness to uncertainty in the sail lightness number.

2. Elliptic three-body problem for RCD solar sail

2.1. Equations of motion for the SSER3BP

The non-dimensional equations of motion of the SSER3BP are expressed in a pulsating-rotating frame (Szebehely, 1967; Biggs et al., 2008)

$$\begin{aligned} x'' - 2y' &= \tfrac{1}{1+e\cos f}\left(x - \tfrac{1-\mu}{r_1^3}(x+\mu) - \tfrac{\mu}{r_2^3}(x-1+\mu) + a_x\right) \\ y'' + 2x' &= \tfrac{1}{1+e\cos f}\left(y - \tfrac{1-\mu}{r_1^3}y - \tfrac{\mu}{r_2^3}y + a_y\right) \\ z'' &= \tfrac{1}{1+e\cos f}\left(-ze\cos f - \tfrac{1-\mu}{r_1^3}z - \tfrac{\mu}{r_2^3}z + a_z\right) \end{aligned} \tag{1}$$

where the true anomaly f is the independent variable and the prime $(\cdot)'$ denotes the derivative with respect to f. $x = X/R_{12}$, $y = Y/R_{12}$, $z = Z/R_{12}$ are the non-dimensionalized position coordinates with respect to the Sun-Earth barycenter, where X, Y and Z are the dimensional position coordinates and R_{12} is the time-varying distance between the two primaries. e is the eccentricity. r_1 and r_2 are the distances from the solar sail to the first and the second primary, respectively, which are given by $r_1 = \sqrt{(x+\mu)^2 + y^2 + z^2}$ and $r_2 = \sqrt{(x-1+\mu)^2 + y^2 + z^2}$. a_x, a_y and a_z are the solar radiation acceleration components. μ is the ratio of the smaller primary mass to the total mass of the two primaries, which for the Sun-Earth system is, $\mu = 3.04 \times 10^{-6}$.

Eq. (1) can be expressed in the following vectorial form

$$\boldsymbol{r''} + 2\boldsymbol{\omega} \times \boldsymbol{r'} = \frac{1}{1 + e\cos f}\left(\frac{\partial U}{\partial \boldsymbol{r}} + \boldsymbol{a}\right) \tag{2}$$

where $\boldsymbol{r} = [x, y, z]^T$, $\boldsymbol{\omega} = [0, 0, 1]^T$, $\boldsymbol{a} = [a_x, a_y, a_z]^T$. The potential function U is defined by the equation

$$U = \left[\frac{1}{2}(x^2 + y^2 - z^2 e\cos f) + \frac{1-\mu}{r_1} + \frac{\mu}{r_2}\right] \tag{3}$$

2.2. Force model of RCD solar sail

When a solar photon intersects the solar sail surface, it can be either reflected, absorbed or transmitted. The probability for each of these events are denoted by ρ_r, ρ_a and ρ_t, respectively where:

$$\rho_r + \rho_a + \rho_t = 1 \tag{4}$$

where ρ_r can be further divided into two parts $\rho_r = \rho_s + \rho_d$, where ρ_s and ρ_d denote the probability for specular reflection and diffusion, respectively. Usually, the transmission can be neglected. Therefore, Eq. 4 can be expressed as

$$\rho_a + \rho_s + \rho_d = 1 \tag{5}$$

The total solar radiation acceleration, which is non-dimensionalized by the same transformation as the equations of motion, can be written as (McInnes, 1999; Fu et al., 2016)

$$\boldsymbol{a} = \frac{1}{2}\beta\frac{1-\mu}{r_1^2}\left(\boldsymbol{s}\cdot\boldsymbol{n}\right)\left[(1-\rho_s)\boldsymbol{s} + \left(2\rho_s\left(\boldsymbol{s}\cdot\boldsymbol{n}\right) + \rho_d B_f + \rho_a\frac{\varepsilon_f B_f - \varepsilon_b B_b}{\varepsilon_f + \varepsilon_b}\right)\boldsymbol{n}\right] \tag{6}$$

where $\boldsymbol{n}$ and $\boldsymbol{s}$ are the unit vectors of the sail normal and the Sun-sail line, respectively; β is the lightness number; ε_f and ε_b are the front and back emissivities; B_f and B_b are the front and back non-Lambertian coefficients. For simplicity, we express Eq. (6) as

$$\boldsymbol{a} = \beta\frac{1-\mu}{r_1^2}\left(M\boldsymbol{s} + N\boldsymbol{n}\right) \tag{7}$$

where

$$\begin{aligned} M &= \tfrac{1}{2}\left(\boldsymbol{s}\cdot\boldsymbol{n}\right)\left(1-\rho_s\right) \\ N &= \tfrac{1}{2}\left(\boldsymbol{s}\cdot\boldsymbol{n}\right)\left(2\rho_s\left(\boldsymbol{s}\cdot\boldsymbol{n}\right)+\rho_d B_f+\rho_a\tfrac{\varepsilon_f B_f-\varepsilon_b B_b}{\varepsilon_f+\varepsilon_b}\right) \end{aligned} \tag{8}$$

An RCD can switch its reflection properties from one state to another state. In this paper, the diffusion mode RCD is considered, which can switch between a specular state and a diffusive state. The parameters in McInnes (1999) are used for the specular state, $\rho_a = 0.12$, $\rho_{s1} = 0.8272$, $\rho_{d1} = 0.0528$, $\varepsilon_f = 0.05$, $\varepsilon_b = 0.55$, $B_f = 0.79$, $B_b = 0.55$. For the diffusive state, it is assumed that all specular reflection transforms to diffusion, that is $\rho_{s2} = 0$, $\rho_{d2} = 0.88$. The reflection properties of the RCD in the specular state are assumed to be the same as that of the sail surface without RCDs. We define the RCD ratio σ as the ratio of the area in the diffusive state to the total sail area. The total solar radiation acceleration consists of the following two parts:

$$\boldsymbol{a} = \boldsymbol{a}_1 + \boldsymbol{a}_2 \tag{9}$$

$$\boldsymbol{a}_1 = \beta\left(1-\sigma\right)\frac{1-\mu}{r_1^2}\left(M_1\boldsymbol{s}+N_1\boldsymbol{n}\right) \tag{10}$$

$$\boldsymbol{a}_2 = \beta\sigma\frac{1-\mu}{r_1^2}\left(M_2\boldsymbol{s}+N_2\boldsymbol{n}\right) \tag{11}$$

where the subscript 1 of $\boldsymbol{a}$, M and N denotes the specular state, and the subscript 2 denotes the diffusive state. Note that the magnitude and direction of the solar radiation acceleration can be physically adjusted by changing σ. In this paper, we assume that 10% of the sail surface is equipped with RCDs, that is, the range of σ is $0 \leq \sigma \leq 0.1$.

In order to express the solar radiation acceleration in the pulsating rotating frame, two sail angles are used to describe the orientation of the sail. There are two definitions of the sail angles in the literature. The first definition uses the cone angle and clock angle (McInnes, 1999; Gong et al., 2014) while the second definition uses the pitch angle and azimuth angle (Biggs et al., 2009; Biggs and McInnes, 2009). However, the first definition has a drawback that when the

cone angle is zero, the clock angle has no influence on the sail acceleration. Therefore, the pitch angle γ and the azimuth angle δ are used in this paper. Fig. 1 shows the definition of these two angles, where x, y, z are the axes of the pulsating rotating frame. γ is defined as the angle between the sail-normal and the x-y plane, while δ is defined as the angle between the projection of the sail normal in the x-y plane and the x-axis.

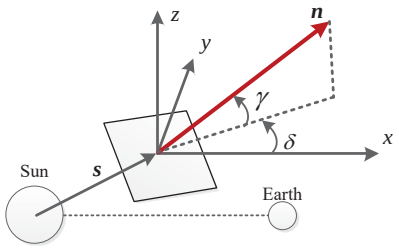

Figure 1: Definition of sail angles

The components of $\boldsymbol{n}$ in the pulsating rotating frame are

$$\boldsymbol{n} = [\cos\gamma\cos\delta,\ \ \cos\gamma\sin\delta,\ \ \sin\gamma]^T \tag{12}$$

2.3. Equations of motion for reference orbit

For the reference orbit design, the sail normal is considered to be orientated along the Sun-sail line, and the corresponding sail parameters are called the nominal sail parameters, which are denoted by a subscript e. In this case, Eq. (9) can be expressed as

$$\boldsymbol{a} = \beta K_e \frac{1-\mu}{r_1^2}\boldsymbol{n}_e \tag{13}$$

where

$$\boldsymbol{n}_e = \boldsymbol{s} = [x+\mu, y, z]^T \Big/ r_1 \tag{14}$$

$$K_e = (1-\sigma_e)\,K_1 + \sigma_e K_2 \tag{15}$$

$$K_1 = \frac{1}{2}\left(1 + \rho_{s1} + \rho_{d1}B_f + \rho_a \frac{\varepsilon_f B_f - \varepsilon_b B_b}{\varepsilon_f + \varepsilon_b}\right) \tag{16}$$

$$K_2 = \frac{1}{2}\left(1 + \rho_{s2} + \rho_{d2}B_f + \rho_a \frac{\varepsilon_f B_f - \varepsilon_b B_b}{\varepsilon_f + \varepsilon_b}\right) \tag{17}$$

σ_e is set to 0.05, i.e., half of RCDs are in the specular state while the other half are in the diffusive state. Substituting Eq. (14) into Eq. (12), the nominal sail angles can be solved by

$$\begin{aligned} \gamma_e &= \arcsin\left(\tfrac{z}{r_1}\right) \\ \delta_e &= \arctan\left(\tfrac{y}{x+\mu}\right) \end{aligned} \tag{18}$$

Substituting Eq. (13) into Eq. (1), the equations of motion are transformed to

$$\begin{aligned} x'' - 2y' &= \tfrac{1}{1+e\cos f}\left(x - \tfrac{(1-\mu)(1-\beta K_e)}{r_1^3}(x+\mu) - \tfrac{\mu}{r_2^3}(x-1+\mu)\right) \\ y'' + 2x' &= \tfrac{1}{1+e\cos f}\left(y - \tfrac{(1-\mu)(1-\beta K_e)}{r_1^3}y - \tfrac{\mu}{r_2^3}y\right) \\ z'' &= \tfrac{1}{1+e\cos f}\left(-ze\cos f - \tfrac{(1-\mu)(1-\beta K_e)}{r_1^3}z - \tfrac{\mu}{r_2^3}z\right) \end{aligned} \tag{19}$$

The vectorial form of Eq. (19) is

$$\boldsymbol{r''} + 2\boldsymbol{\omega} \times \boldsymbol{r'} = \frac{1}{1+e\cos f}\frac{\partial \bar{U}}{\partial \boldsymbol{r}} \tag{20}$$

where

$$\bar{U} = \left[\frac{1}{2}(x^2 + y^2 - z^2 e\cos f) + \frac{(1-\mu)(1-\beta K_e)}{r_1} + \frac{\mu}{r_2}\right] \tag{21}$$

It can be seen from the third equation of Eq. (19) that the AEPs only exist in the x-y plane due to the term $\cos f$. In this paper, we focus on the collinear AEPs (L_1, L_2, and L_3), which can be obtained by setting $x'' = y'' = z'' = x' = y' = y = z = 0$ in Eq. (19) and then solving for x. According to Eq. (19), the collinear AEPs in the SSER3BP are the same as those in the SSCR3BP. Fig. 2 shows the 3 collinear AEPs with β changing from 0 to 0.5. The AEPs shift towards the Sun with increasing β. The families of AHOs in this paper are around these AEPs.

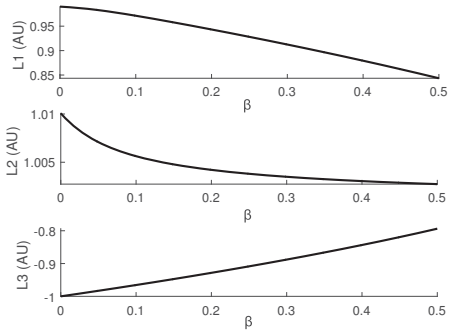

Figure 2: The x-coordinate of the collinear AEPs for varying β

3. A strategy for generating families of AHOs in the SSER3BP

3.1. Procedure for generating AHOs

Since the ER3BP is non-autonomous, any periodic orbit must have a period equal to an integer multiple of one year, i.e. $2n\pi$ (Broucke, 1969; Hou and Liu, 2011; Campagnola et al., 2008), where n is an arbitrary positive integer and 2π is the non-dimensional time corresponding to one year. The procedure to generate AHOs in the SSER3BP is to numerically continue them from an AHO computed initially in the SSCR3BP. However, the periods of AHOs around the collinear L_1 and L_2 AEPs in the Sun-Earth SSCR3BP are always less than 2π, and thus it is not possible to find a qualified seed orbit from the classic AHOs around the collinear L_1 and L_2 AEPs in the Sun-Earth SSCR3BP. However, an infinite number of AHOs with periods equal to fractions of one year, i.e. $2n\pi/m$, where m is an arbitrary positive integer, can be used to construct m-revolution AHOs whose periods equal $2n\pi$ by computing single-revolution AHOs for m periods. These m-revolution AHOs are then used as seeds to compute AHOs in the SSER3BP using numerical continuation, with the eccentricity and the lightness number used as the continuation parameters.

This procedure is explained in detail in sub-sections 3.2 to 3.5.

3.2. A modified 3rd order approximation for the SSCR3BP

Richardson (1980a,c) proposed a 3rd order solution to approximate halo

orbits around the collinear Lagrange points for the classical CR3BP. McInnes (2000) extended Richardson's method to the SSCR3BP for a perfectly reflecting solar sail. In this paper, we extend McInnes' method to the case of a non-perfectly reflecting RCD solar sail. This enables an initial guess to compute an initial single-revolution AHO in the SSCR3BP with period $2n\pi/m$.

Recall Richardson's 3rd order halo orbit approximation. If the Lagrangian for the motion of a spacecraft relative to the collinear equilibrium points can be expressed by a Legendre polynomial as

$$L = \frac{1}{2}\left(\boldsymbol{\rho'}\cdot\boldsymbol{\rho'}\right) + \sum_{n=2}^{\infty} c_n \rho^n P_n(x/\rho) \tag{22}$$

The 3rd order solution for periodic motion near the collinear equilibrium points can be found to be

$$\begin{aligned}
\tilde{x} &= a_{21}A_x^2 + a_{22}A_z^2 - A_x\cos\tau_1 + (a_{23}A_x^2 + a_{24}A_z^2)\cos 2\tau_1 + (a_{31}A_x^3 - a_{32}A_xA_z^2)\cos 3\tau_1 \\
\tilde{y} &= kA_x\sin\tau_1 + (b_{21}A_x^2 - b_{22}A_z^2)\sin 2\tau_1 + (b_{31}A_x^3 - b_{32}A_xA_z^2)\sin 3\tau_1 \\
\tilde{z} &= \delta_n A_z\cos\tau_1 + \delta_n d_{21}A_xA_z(\cos 2\tau_1 - 3) + \delta_n(d_{32}A_zA_x^2 - d_{31}A_z^3)\cos 3\tau_1
\end{aligned} \tag{23}$$

where $\tilde{x}$, $\tilde{y}$, $\tilde{z}$ are the position coordinates relative to the equilibrium points. A_x and A_z are the amplitudes in the x-direction and the z-direction, respectively. The definition of the other parameters can be found in Richardson (1980a).

McInnes (2000) transformed the Lagrangian for the motion of a perfectly reflecting solar sail around the collinear AEPs into the Legendre polynomial in Eq. (22). In this paper, based on McInnes (2000), the Lagrangian for the motion of RCD solar sail around the collinear AEPs is transformed into the Legendre polynomial in Eq. (22). The RCD solar sail model in Eq.(13) is used in an analogous way to derive the Lagrangian

$$\begin{aligned}
L &= \tfrac{1}{2}\left(\boldsymbol{\rho'}\cdot\boldsymbol{\rho'}\right) + (1-\mu)\left(1-\beta K_e\right)\left(\tfrac{1}{|\boldsymbol{r}_1-\boldsymbol{\rho}|} - \tfrac{\boldsymbol{r}_1\cdot\boldsymbol{\rho}}{|\boldsymbol{r}_1|^3}\right) + \mu\left(\tfrac{1}{|\boldsymbol{r}_2-\boldsymbol{\rho}|} - \tfrac{\boldsymbol{r}_2\cdot\boldsymbol{\rho}}{|\boldsymbol{r}_2|^3}\right) \\
&= \tfrac{1}{2}\left(\boldsymbol{\rho'}\cdot\boldsymbol{\rho'}\right) + \sum_{n=2}^{\infty} c_n\rho^n P_n(x/\rho)
\end{aligned} \tag{24}$$

where

$$c_n = \left[\frac{(-1)^n (1-\mu)(1-\beta K_e)}{(1-\gamma_L)^{n+1}} + \frac{\mu}{\gamma_L^{n+1}} \right], \qquad \text{(for } L_1\text{)} \tag{25}$$

$$c_n = \left[\frac{(-1)^n (1-\mu)(1-\beta K_e)}{(1+\gamma_L)^{n+1}} + \frac{(-1)^n \mu}{\gamma_L^{n+1}} \right], \quad \text{(for } L_2\text{)} \tag{26}$$

$$c_n = \left[\frac{(1-\mu)(1-\beta K_e)}{\gamma_L^{n+1}} + \frac{\mu}{(1+\gamma_L)^{n+1}} \right], \qquad \text{(for } L_3\text{)} \tag{27}$$

where K_e is the nominal K given in Eq. (15), γ_L is the ratio of the distance between the AEPs and the nearest primary to the distance between the primaries. For a perfectly reflecting solar sail, i.e. $K_e = 1$, Eq. (24) reduces to the Lagrangian in McInnes (2000).

The new coefficients obtained by Eq. (25–27) can be substituted into the expressions in Appendix I of Richardson (1980a) or Appendix B of McInnes (2000) to obtain the approximate solutions for periodic AHOs near the collinear AEPs.

3.3. Period of AHOs in the SSCR3BP

The initial goal is to compute AHOs with period $2n\pi/m$ in the SSCR3BP. In the 3rd order approximation, the non-dimensional period T^* is given by

$$T^* = 2\pi/\lambda \tag{28}$$

$$\lambda^4 + (c_2 - 2)\lambda^2 - (c_2 - 1)(1 + 2c_2) = 0 \tag{29}$$

However, the non-dimensionalization for T^* is not the same as that in the SSCR3BP where the time is non-dimensionalized by $\tau = n_1 t$ (t is the dimensional time and n_1 is the mean angular velocity of the Sun-Earth system) so that 2π corresponds to one year. Therefore, it is required to transform T^* to T

which is the period non-dimensionalized as same as that in the SSCR3BP, that is

$$T = T^*/\omega \tag{30}$$

$$\omega = 1 + \omega_1 + \omega_2 \tag{31}$$

$$\omega_1 = 0,\ \omega_2 = s_1 A_x^2 + s_2 A_z^2 \tag{32}$$

where the coefficients s_1 and s_2 can be found in Richardson (1980a). T depends on both β and A_z. Fig. 3 shows the period T of the Sun-Earth L_1 AHOs with respect to β and A_z. The results in the cases of L_2 and L_3 can be obtained in the same way. It can be seen that, the periods T are always less than 2π, i.e. $T = 2n\pi/m < 2\pi$. Thus, m must be larger than 1, that is, only multi-revolution L_1 AHOs exist in the Sun-Earth SSER3BP.

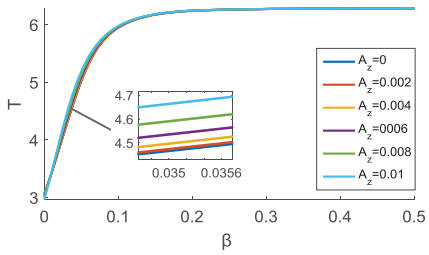

Figure 3: Period T of L_1 AHOs with respect to β and A_z

3.4. Differential Correction of the analytical approximation

Although the 3rd order solution provides an initial guess for integrating the nonlinear equation of motion, it is not accurate enough to obtain a closed periodic orbit in the full non-linear dynamics. Therefore, a differential correction is required. For an AHO with period T, it perpendicularly crosses the x-z plane

at $t = 0$ and $t = T/2$. The initial state is set as

$$\boldsymbol{X}(0) = [x_0,\ 0,\ z_0,\ 0,\ V_{y0},\ 0]^T \tag{33}$$

The state at $t = T/2$ can be obtained by integrating

$$\boldsymbol{X}(T/2) = [x_{T/2},\ \delta y,\ z_{T/2},\ \delta V_x,\ V_{y,T/2},\ \delta V_z]^T \tag{34}$$

where δy, δV_x and δV_z are the errors in y, V_x and V_z at $t = T/2$ which can be used to correct the initial values for x_0, z_0 and V_{y0} by the following formula

$$\begin{bmatrix} \delta y \\ \delta V_x \\ \delta V_z \end{bmatrix} = \begin{bmatrix} \boldsymbol{\Phi}_{T/2}(2,1) & \boldsymbol{\Phi}_{T/2}(2,3) & \boldsymbol{\Phi}_{T/2}(2,5) \\ \boldsymbol{\Phi}_{T/2}(4,1) & \boldsymbol{\Phi}_{T/2}(4,3) & \boldsymbol{\Phi}_{T/2}(4,5) \\ \boldsymbol{\Phi}_{T/2}(6,1) & \boldsymbol{\Phi}_{T/2}(6,3) & \boldsymbol{\Phi}_{T/2}(6,5) \end{bmatrix} \begin{bmatrix} \delta x_0 \\ \delta z_0 \\ \delta V_{y0} \end{bmatrix} \tag{35}$$

where $\boldsymbol{\Phi}_{T/2}$ is the state-transition matrix from $t = 0$ to $t = T/2$. This process is repeated until the values for δy, δV_x, δV_z are smaller than a given tolerance ε.

3.5. Numerical results: families of AHOs in the SSER3BP

The families of AHOs in the SSER3BP can be generated using a numerical continuation method. For a fixed step continuation (Heiligers et al., 2016; Yuan et al., 2018; Biggs et al., 2008), the increment of the continuation parameter is constant, which needs to be very small to avoid diverging and leads to very long computation time. In this section, a variable step numerical continuation is provided which significantly reduce the computation time.

It is known that if the increment of the continuation parameter is too large, the differential correction may not converge, or it will require a large amount of iterations to converge. Therefore, if the number of iterations is large, it implies that the increment of the continuation parameter should be reduced; while if the number of iterations is small, it implies that the increment of the continuation parameter can be increased. As illustrated in Fig. 4, i is the number of iterations of the differential correction, and δ_a is the increment of

the continuation parameter a. If $i < i_1$, δ_a would be increased ($k_1 > 1$) in the next step; else if $i > i_2$, δ_a would be decreased ($k_2 < 1$); else, δ_a would keep unchanged. i_1 and i_2 are two threshold parameters chosen by trial, in this paper, $i_1 = 5$ and $i_2 = 10$.

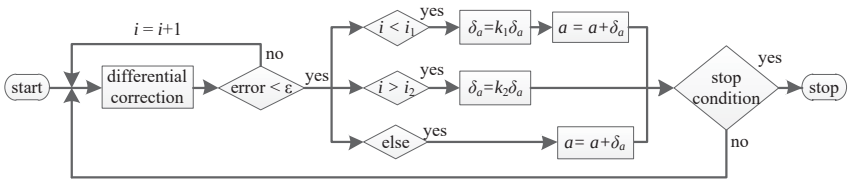

Figure 4: Variable step numerical continuation

There are two families of AHOs in the SSER3BP emanating from each AHO in the SSCR3BP (Campagnola et al., 2008; Hou and Liu, 2011). If m is odd, the two families are called the periapsis family and apoapsis family, depending on whether the first perpendicular crossing occurs when the Earth is at the periapse ($f(0) = 0$) or at the apoapse ($f(0) = \pi$). In this case, the two perpendicular crossing points are at two sides of the orbit (see the red dots in Fig. 5). If m is even, the two families are called the left family and right family, depending on whether the first perpendicular crossing occurs at the left apse or the right apse in the x-y plane. In this case, the two perpendicular crossing points are at the same side of the orbit (see the red dots in Fig. 6).

The results of two families of the L_1 AHOs in the Sun-Earth SSER3BP are given as examples. One is the left family of 2-revolution southern AHOs with period 2π as shown in Fig. 7. Another is the periapsis family of 3-revolution southern AHOs with period 4π as shown in Fig. 8. The other families can be obtained in the same way. Note that these families consist of the AHOs with the same period $T = 2n\pi$, the same number of revolutions m and the same eccentricity e=0.0167, but different β and amplitude, which are different from the families in the classical CR3BP or ER3BP.

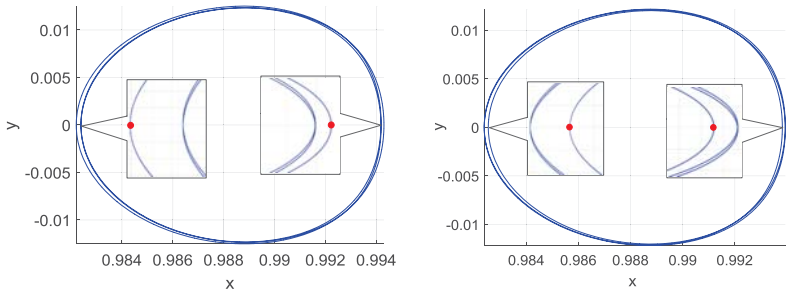

(a) $f(0) = 0$ (b) $f(0) = \pi$

Figure 5: Two 3-revolution orbits in the SSER3BP with period 4π emanating from the same single-revolution orbit in the SSCR3BP with period $4\pi/3$

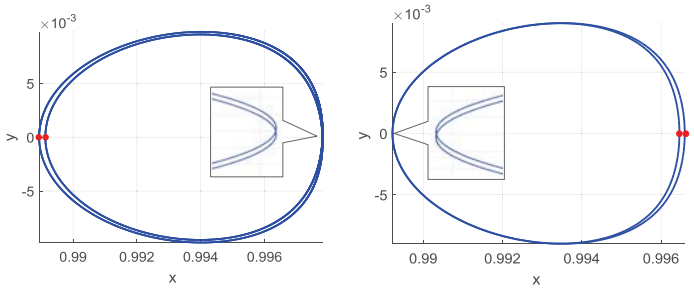

(a) Left crossing (b) Right crossing

Figure 6: Two 2-revolution orbits in the SSER3BP with period 2π emanating from the same single-revolution orbit in the SSCR3BP with period π

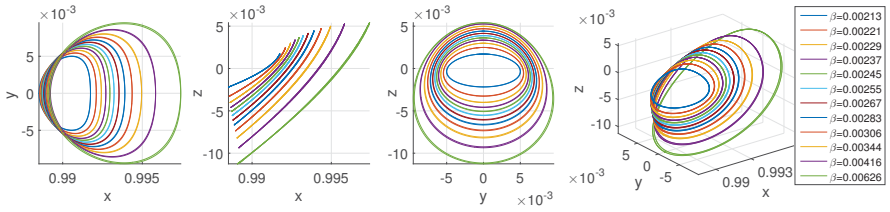

Figure 7: The left family of 2-revolution southern L_1 AHOs with period 2π

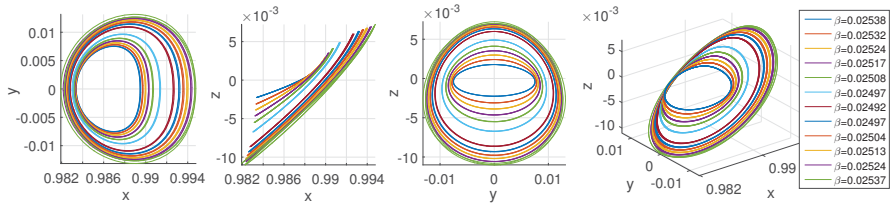

Figure 8: The periapsis family of 3-revolution southern L_1 AHOs with period 4π

4. Stability analysis

The linear stability of periodic orbits can be deduced by computing the eigenvalues of the monodromy matrix $\boldsymbol{M} = \boldsymbol{\Phi}(T, t_0)$, where $\boldsymbol{\Phi}(T, t_0)$ is the state transition matrix for one period. A periodic orbit is stable if all the eigenvalues are on the unit circle. The stability analysis in this section involves to the families of AHOs in section 3.5.

In these cases, there are 3 pairs of eigenvalues. The first pair consists of two conjugate complex eigenvalues. The second pair consists of two reciprocal real eigenvalues and the third pair comes from the unit eigenvalue $\lambda = 1$ in the CR3BP. Due to the eccentricity, the unit eigenvalues move onto either the real axis or the unit circle in the ER3BP (Broucke, 1969; Campagnola et al., 2008). However, since the eccentricity here is very small, the third pair of eigenvalues are always in the vicinity of the point $(1, 0i)$ which are called here the quasi-unit eigenvalues. Fig. 9 shows the variations of the 3 pairs of eigenvalues with the orbit amplitude increasing.

The out-of-plane motion depends on the pair of complex eigenvalues (the red arrows in Fig. 9). As shown in Fig. 9, as the amplitude increases, this pair of eigenvalues moves from the point $(1, 0i)$ along the unit circle in opposite directions, and finally return to the point $(1, 0i)$. When they cross the real axis at the point $(-1, 0i)$, a bifurcation occurs. This bifurcation changes the nature of the families of 3-revolution AHOs, that is, before the bifurcation, β decreases as the amplitude A_z increases, while after the bifurcation it increases with A_z (see Fig. 10b). However, for the families of 2-revolution AHOs, β always increases

with A_z (see Fig. 10a). Since this pair of eigenvalues is always on the unit circle, it can be inferred that the out-of-plane motion is neutrally stable.

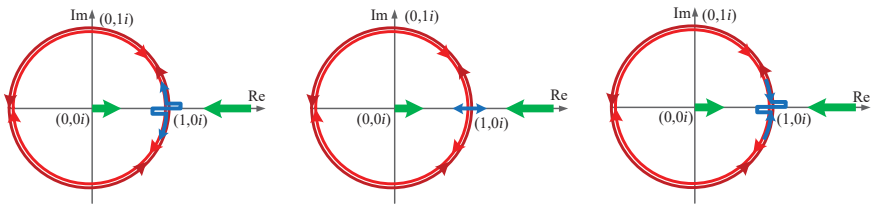

(a) (b) (c)

Figure 9: The variations of the 3 pairs of eigenvalues with increasing orbit amplitude. a) the left family of the 2-revolution AHOs; b) the right family of the 2-revolution AHOs; c) the periapsis family and the apoapsis family of the 3-revolution AHOs

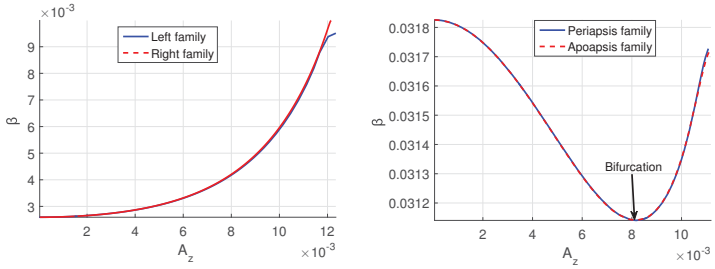

(a) (b)

Figure 10: The relationship between β and A_z. a): families of 2-revolution AHOs; b) families of 3-revolution AHOs

The in-plane motion depends on the pair of real eigenvalues (the green arrows in Fig. 9) and the pair of quasi-unit eigenvalues (the blue arrows in Fig. 9). However, the quasi-unit eigenvalues are always in the vicinity of the point (1, $0i$) and the deviation is smaller than 0.01, while the real eigenvalues are far from the unit circle. Therefore, the in-plane motion mainly depends on the real eigenvalues.

As shown in Fig. 9, as the orbit amplitude increases, the pair of real eigenvalues move towards the point (1, $0i$) from two sides. We introduce the stability

index defined by Howell (1984), that is

$$\upsilon = (\lambda + 1/\lambda)/2 \tag{36}$$

where λ and $1/\lambda$ are the pair of real eigenvalues. The smaller υ is, the more stable the orbit is. Fig. 11 illustrates υ with respect to the amplitude A_z. It can be seen that υ decreases as the amplitude A_z increases, that is, the bigger the amplitude is, the more stable the orbit is. However, υ is always larger than 1, which means the in-plane motion is always unstable.

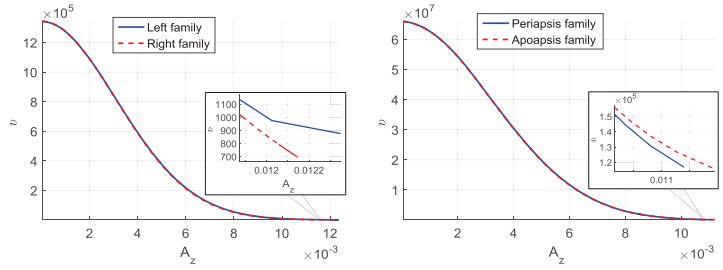

(a) (b)

Figure 11: The relationship between υ and A_z. a): families of 2-revolution AHOs; b) families of 3-revolution AHOs

Simulations are used to verify the stability analysis above. An injection error of 150km in position and 0.03m/s in velocity is considered. Two orbits with $A_z = 0.002$ (orbit 1) and $A_z = 0.009$ (orbit 2) are chosen from the 3-revolution family. The stability indices υ are 5.3×10^7 and 1.2×10^6, respectively. The orbits are simulated for one revolution ($T = 4\pi/3$).

Fig. 12 and Fig. 13 show the position errors and velocity errors of orbit 1 and orbit 2, respectively, where a)–f) are the cases for which the error is added to the initial position components x_0, y_0, z_0 and the initial velocity components V_{x0}, V_{y0}, V_{z0}, respectively. It can be seen that the motion in the x-y plane diverges with time, while the motion along the z-axis (out-of-plane) oscillates in the vicinity of zero, which is consistent with the features of the eigenvalues mentioned above. It is also shown that the bigger υ is, the faster the in-plane

motion diverges.

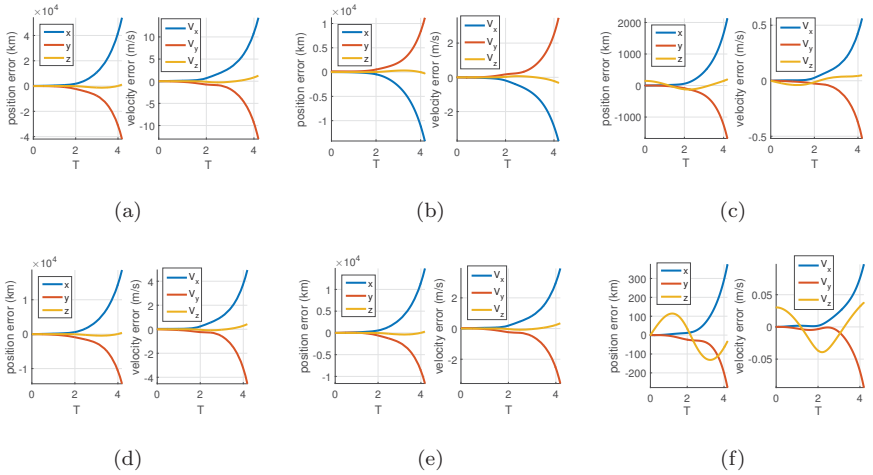

Figure 12: Position errors and velocity errors of orbit 1 ($\upsilon = 5.3 \times 10^7$). a)–f) are the cases with errors in the x_0, y_0, z_0 , V_{x0}, V_{y0} and V_{z0}, respectively

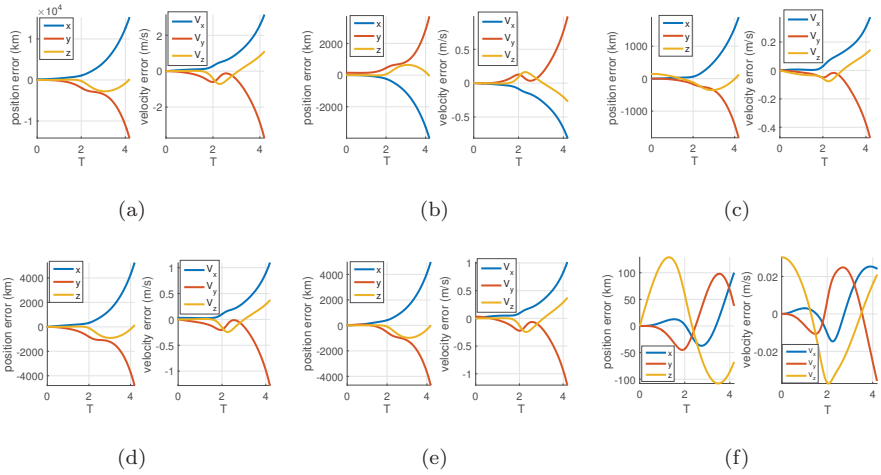

Figure 13: Position errors and velocity errors of orbit 2 ($\upsilon = 1.2 \times 10^6$). a)–f) are the cases with errors in the x_0, y_0, z_0 , V_{x0}, V_{y0} and V_{z0}, respectively

5. Station keeping

The families of multi-revolution AHOs in section 3 are unstable. Therefore, station-keeping is required. The periodic AHOs in section 3 are used as the reference orbits in this section.

5.1. Linear model for control

In this section, the classical LQR (Kirk, 2004) method is used to design the control law. The linearized model with respect to the reference orbit is expressed as the form of state space equation.

$$\dot{\boldsymbol{X}} = \boldsymbol{A}\boldsymbol{X} + \boldsymbol{B}\boldsymbol{u} \tag{37}$$

where the state vector $\boldsymbol{X} = [\Delta x,\ \Delta y,\ \Delta z,\ \Delta V_x,\ \Delta V_y,\ \Delta V_z]^T$ is the deviation of positions and velocities relative to the reference orbit $\boldsymbol{\Gamma}$. $\boldsymbol{A}$ and $\boldsymbol{B}$ are given by

$$\boldsymbol{A} = \begin{bmatrix} \boldsymbol{0}_{3\times3} & \boldsymbol{I}_{3\times3} \\ \frac{1}{1+e\cos f}\frac{\partial^2 \bar{U}}{\partial \boldsymbol{r}\partial \boldsymbol{r}}\Big|_{\substack{\boldsymbol{X}=\boldsymbol{\Gamma}\\ \boldsymbol{u}=\boldsymbol{u}_e}} & \boldsymbol{\Omega} \end{bmatrix} \tag{38}$$

$$\boldsymbol{\Omega} = \begin{bmatrix} 0 & 2 & 0 \\ -2 & 0 & 0 \\ 0 & 0 & 0 \end{bmatrix} \tag{39}$$

$$\boldsymbol{B} = \begin{bmatrix} \boldsymbol{0}_{3\times3} \\ \frac{1}{1+e\cos f}\frac{\partial \boldsymbol{a}}{\partial \boldsymbol{u}}\Big|_{\substack{\boldsymbol{X}=\boldsymbol{\Gamma}\\ \boldsymbol{u}=\boldsymbol{u}_e}} \end{bmatrix} \tag{40}$$

For a normal solar sail, the control vector $\boldsymbol{u} = [\Delta\gamma,\ \Delta\delta]^T$ is the deviation of the sail angles relative to the nominal values. For an RCD solar sail, $\boldsymbol{u} = [\Delta\gamma,\ \Delta\delta,\ \Delta\sigma]^T$, where $\Delta\sigma$ is the deviation of σ relative to the nominal value.

The partial derivatives in Eq. (40) are given by

$$\begin{cases} \frac{\partial \boldsymbol{a}}{\partial \sigma} = \beta \left(K_2 - K_1\right) \frac{1-\mu}{r_1^2} \boldsymbol{n} \\ \frac{\partial \boldsymbol{a}}{\partial \gamma} = \beta \frac{1-\mu}{r_1^2} \left[(1-\sigma_e) \left(\frac{\partial M_1}{\partial \gamma} \boldsymbol{s} + \frac{\partial N_1}{\partial \gamma} \boldsymbol{n} + \frac{\partial \boldsymbol{n}}{\partial \gamma} N_1 \right) + \sigma_e \left(\frac{\partial M_2}{\partial \gamma} \boldsymbol{s} + \frac{\partial N_2}{\partial \gamma} \boldsymbol{n} + \frac{\partial \boldsymbol{n}}{\partial \gamma} N_2 \right) \right] \\ \frac{\partial \boldsymbol{a}}{\partial \delta} = \beta \frac{1-\mu}{r_1^2} \left[(1-\sigma_e) \left(\frac{\partial M_1}{\partial \delta} \boldsymbol{s} + \frac{\partial N_1}{\partial \delta} \boldsymbol{n} + \frac{\partial \boldsymbol{n}}{\partial \delta} N_1 \right) + \sigma_e \left(\frac{\partial M_2}{\partial \delta} \boldsymbol{s} + \frac{\partial N_2}{\partial \delta} \boldsymbol{n} + \frac{\partial \boldsymbol{n}}{\partial \delta} N_2 \right) \right] \end{cases} \tag{41}$$

where

$$\begin{aligned} &\frac{\partial M_i}{\partial \gamma} = \frac{1}{2} \left(\boldsymbol{s} \cdot \frac{\partial \boldsymbol{n}}{\partial \gamma} \right) (1 - \rho_{si}), \ i{=}\, 1, 2 \\ &\frac{\partial M_i}{\partial \delta} = \frac{1}{2} \left(\boldsymbol{s} \cdot \frac{\partial \boldsymbol{n}}{\partial \delta} \right) (1 - \rho_{si}), \ i{=}\, 1, 2 \\ &\frac{\partial N_i}{\partial \gamma} = \frac{1}{2} \left(\boldsymbol{s} \cdot \frac{\partial \boldsymbol{n}}{\partial \gamma} \right) \left(4\rho_{si} \left(\boldsymbol{s} \cdot \boldsymbol{n} \right) + \rho_{di} B_f + \rho_a \frac{\varepsilon_f B_f - \varepsilon_b B_b}{\varepsilon_f + \varepsilon_b} \right), \ i{=}\, 1, 2 \\ &\frac{\partial N_i}{\partial \delta} = \frac{1}{2} \left(\boldsymbol{s} \cdot \frac{\partial \boldsymbol{n}}{\partial \delta} \right) \left(4\rho_{si} \left(\boldsymbol{s} \cdot \boldsymbol{n} \right) + \rho_{di} B_f + \rho_a \frac{\varepsilon_f B_f - \varepsilon_b B_b}{\varepsilon_f + \varepsilon_b} \right), \ i{=}\, 1, 2 \\ &\frac{\partial \boldsymbol{n}}{\partial \gamma} = [-\sin\gamma_e \cos\delta_e, \ -\sin\gamma_e \sin\delta_e, \ \cos\gamma_e]^T \\ &\frac{\partial \boldsymbol{n}}{\partial \delta} = [-\cos\gamma_e \sin\delta_e, \ \cos\gamma_e \cos\delta_e, \ \sin\gamma_e]^T \end{aligned} \tag{42}$$

5.2. Simulation and Analysis

In this section, simulations are undertaken to analyze the control performance in 3 cases, in which the influence of the eccentricity (case 1), injection errors (case 2), and an error in β (case 3) is investigated respectively. In reality, an error in β is inevitable as it depends on many factors such as the characteristics of the material, the temperature, etc.. In each case, the control performances of the normal solar sail and the RCD sail are compared.

The simulation results depend on several factors: i) the chosen reference orbit; ii) the values for the errors; iii) the maximum RCD ratio, which is relevant to the maximum available control acceleration; iv) the control parameters, i.e. the weight matrices $\boldsymbol{Q}$ and $\boldsymbol{R}$ for LQR. In this paper, the reference orbit is chosen randomly from the families of orbits in Section 3. The injection error and the error in β are set to medium values for effective station-keeping. The maximum RCD ratio is chosen by referring to "IKAROS". The $\boldsymbol{Q}$ and $\boldsymbol{R}$ are tuned by trial and error.

5.2.1. Case 1: influence of eccentricity

In this case, a periodic AHO designed in the SSCR3BP with amplitude $A_z = 0.009$ and lightness number $\beta = 0.0276$ is chosen to be the reference orbit while the equations of motion of the SSER3BP are considered. Fig. 14a and Fig. 14b show the results for the cases of the normal solar sail and the RCD solar sail, respectively. The errors diverge in both cases. $\Delta\sigma$ is always equal to its maximum value. We have tried to adjust the weight matrices $\boldsymbol{Q}$ and $\boldsymbol{R}$, but we cannot obtain stable results. If the whole solar sail surface is equipped with RCDs and the nominal $\sigma_e = 0.5$, i.e. the maximum value for $\Delta\sigma$ is 0.5, the results are shown in Fig. 14c. Although the errors do not diverge, the maximum steady-state position error reaches 1020 km. Therefore, the results in Fig. 14 imply that the influence of eccentricity yields poor station-keeping performance.

5.2.2. Case 2: influence of injection error

In this case, the reference orbit designed in the SSER3BP is chosen from the family of 3-revolution AHOs in section 3, with amplitude $A_z = 0.009$, lightness number $\beta = 0.0276$ and stability index $\upsilon = 1.2 \times 10^6$. An injection error of 150km in position and 0.03m/s in velocity is taken into account. Fig. 15a and Fig. 15b show the results in the cases of the normal solar sail and the RCD solar sail, respectively. The steady-state errors in the two cases are nearly equal. However, the convergence rate of the normal solar sail is obviously slower than that of the RCD solar sail. The convergence time when the positions errors reach within a margin of $\pm$5km in the case of the normal solar sail is 99 days, while in the case of the RCD solar sail, it is 22 days. In addition, in the case of the normal solar sail, the error of y has a distinct overshoot of 82km, while in the case of the RCD solar sail, the overshoot is 20km.

5.2.3. Case 3: influence of error in β

In this case, the same reference orbit as in case 2 is used. A 0.01% error in β is considered. Fig. 16a and Fig. 16b show the results in the cases of the normal solar sail and the RCD solar sail, respectively. In the case of the normal solar

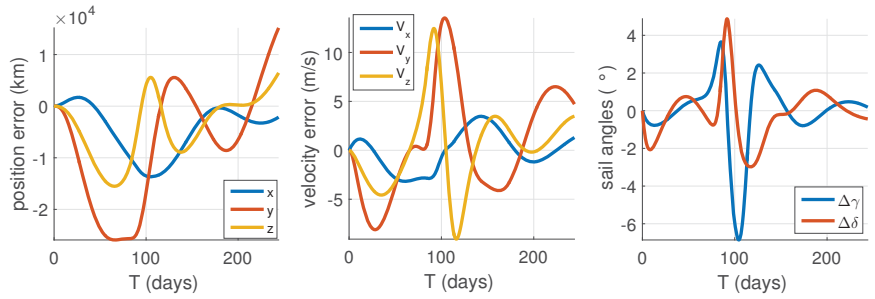

(a) Normal solar sail

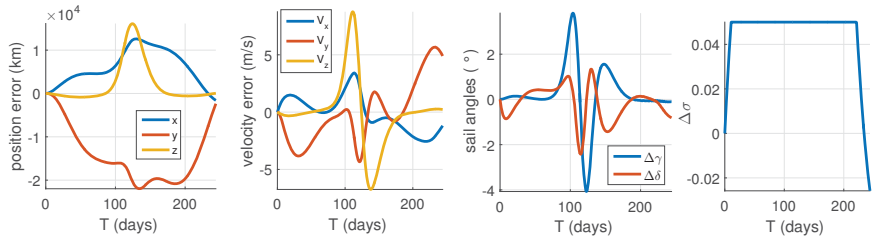

(b) RCD solar sail ($\Delta\sigma_{\max} = 0.05$)

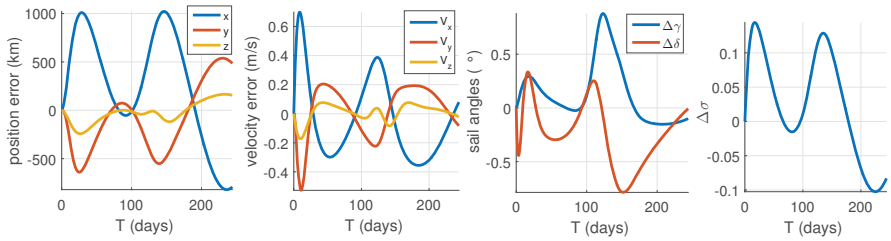

(c) RCD solar sail ($\Delta\sigma_{\max} = 0.5$)

Figure 14: Control performance in the cases using reference orbit in SSCR3BP

sail, both the position errors and the velocity errors are two orders of magnitude bigger than those in the case of the RCD solar sail, which indicates that the RCD solar sail is more robust to the error in β than the normal solar sail. It can be seen from Fig. 16b that $\Delta\sigma$ is nearly a constant of 10^{-3}, which counteracts the error $\delta\beta$ effectively.

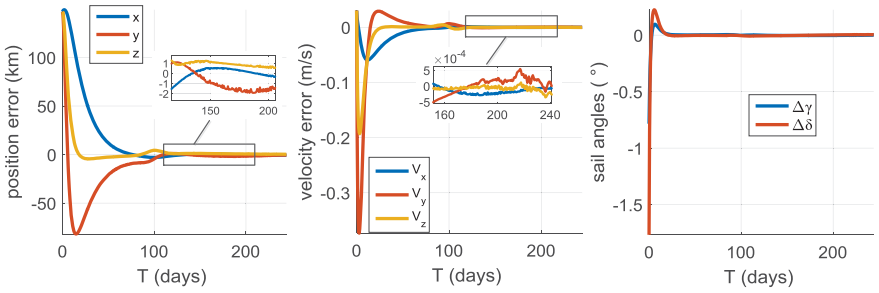

(a) Normal solar sail

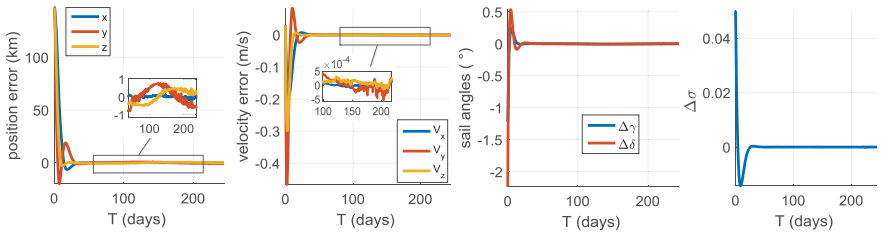

(b) RCD solar sail

Figure 15: Control performance in the cases taking into account the injection error

6. Conclusion

This paper computes families of artificial halo orbits (AHOs) around the collinear artificial equilibrium points in the solar sail elliptic restricted three-body problem (SSER3BP) for a solar sail with reflectivity control devices (RCDs). A modified 3rd order approximation method is used to compute the single-revolution AHOs with periods equal to fractions of one year in the solar sail circular restricted three-body problem (SSCR3BP). The initial m-revolution AHOs with period equal to integer multiples of one year are obtained by computing the single-revolution AHOs for m periods. Then, the families of multi-revolution AHOs in the SSER3BP are generated using a variable step numerical continuation method with the eccentricity and the lightness number as continuation parameters. The linear stability of the 2-revolution family and the 3-revolution family is analyzed and it is shown that the in-plane motion is unstable while

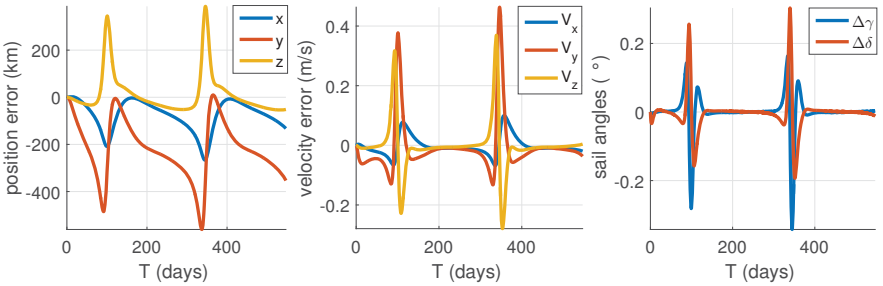

(a) Normal solar sail

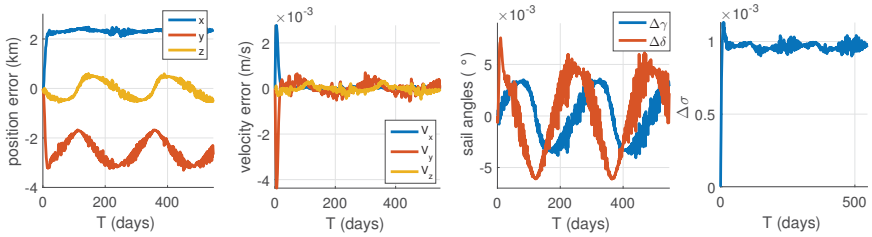

(b) RCD solar sail

Figure 16: Fig. 16 Control performance in the cases taking into account the error in β

the out-of-plane motion is neutrally stable and a bifurcation is identified. Finally, station-keeping for a normal solar sail and an RCD solar sail is designed using LQR control. The simulation results show that the station-keeping performance is poor when trying to track a reference orbit generated in the SSCR3BP, but yields good tracking performance when a reference orbit generated in the SSER3BP is used. In addition, the inclusion of RCD technology is shown to improve station-keeping convergence rates in the presence of injection errors with improved robustness to uncertainty in the sail lightness number.

Acknowledgements

This work was supported by State Administration of Foreign Experts Affairs P. R. China [grant number P180590003].

References

Aliasi, G., Mengali, G., Quarta, A.A., 2013. Artificial lagrange points for solar sail with electrochromic material panels. J. Guid. Control Dyn. 36, 1544–1550. doi:10.2514/1.58167.

Baoyin, H., Mcinnes, C.R., 2006. Solar sail halo orbits at the sun–earth artificial l 1 point. Celest. Mech. Dyn. Astr. 94, 155–171. doi:10.1007/s10569-005-4626-3.

Biggs, J., McInnes, C., Waters, T., 2008. New periodic orbits in the solar sail restricted three body problem, in: 2nd Conference on Nonlinear Science and Complexity, Porto, Portugal.

Biggs, J.D., McInnes, C., 2009. Solar sail formation flying for deep-space remote sensing. J. Spacecraft Rockets 46, 670–678. doi:10.2514/1.42404.

Biggs, J.D., McInnes, C.R., Waters, T., 2009. Control of solar sail periodic orbits in the elliptic three-body problem. J. Guid. Control Dyn. 32, 318–320. doi:10.2514/1.38362.

Biggs, J.D., Negri, A., 2019. Orbit-attitude control in a circular restricted three-body problem using distributed reflectivity devices. J. Guid. Control Dyn. doi:10.2514/1.G004493. published online (in press).

Broucke, R., 1969. Stability of periodic orbits in the elliptic, restricted three-body problem. AIAA J. 7, 1003–1009. doi:10.2514/3.5267.

Campagnola, S., Lo, M., Newton, P., 2008. Subregions of motion and elliptic halo orbits in the elliptic restricted three-body problem, in: Spaceflight mechanics 2008: proceedings of the AAS/AIAA Space Flight Mechanics Meeting, Galveston, Texas.

Cipriano, A., Dei Tos, D.A., Topputo, F., et al., 2018. Orbit design for lumio: The lunar meteoroid impacts observer. Fron. Astron. Space Sci. 5, 1–23. doi:10.3389/fspas.2018.00029.

Dei Tos, D.A., Topputo, F., 2017. Trajectory refinement of three-body orbits in the real solar system model. Adv. Space Res. 59, 2117–2132. doi:10.1016/j.asr.2017.01.039.

Farrés, A., Jorba, À., 2010. Dynamics of a solar sail near a halo orbit. Acta Astronaut. 67, 979–990. doi:10.1016/j.actaastro.2010.05.022.

Farrés, A., Jorba, À., 2011. On the station keeping of a solar sail in the elliptic sun–earth system. Adv. Space Res. 48, 1785–1796. doi:10.1016/j.asr.2011.02.004.

Fu, B., Sperber, E., Eke, F., 2016. Solar sail technology—a state of the art review. Prog. Aerosp. Sci. 86, 1–19. doi:10.1016/j.paerosci.2016.07.001.

Funase, R., Shirasawa, Y., Mimasu, Y., Mori, O., Tsuda, Y., Saiki, T., Kawaguchi, J., 2011. On-orbit verification of fuel-free attitude control system for spinning solar sail utilizing solar radiation pressure. Adv. Space Res. 48, 1740–1746. doi:10.1016/j.asr.2011.02.022.

Gong, S., Li, J., 2015a. Equilibria near asteroids for solar sails with reflection control devices. Astrophys. Space Sci. 355, 213–223. doi:10.1007/s10509-014-2165-7.

Gong, S., Li, J., 2015b. Solar sail periodic orbits in the elliptic restricted three-body problem. Celest. Mech. Dyn. Astr. 121, 121–137. doi:10.1007/s10569-014-9590-3.

Gong, S., Li, J., Simo, J., 2014. Orbital motions of a solar sail around the l 2 earth–moon libration point. J. Guid. Control Dyn. 37, 1349–1356. doi:10.2514/1.G000063.

Gong, S., Macdonald, M., 2019. Review on solar sail technology. Astrodyn. 3, 93–125. doi:10.1007/s42064-019-0038-x.

Heiligers, J., Macdonald, M., Parker, J.S., 2016. Extension of earth-moon libration point orbits with solar sail propulsion. Astrophys. Space Sci. 361, 241. doi:10.1007/s10509-016-2783-3.

Hou, X., Liu, L., 2011. On motions around the collinear libration points in the elliptic restricted three-body problem. Mon. Not. R. Astron. Soc. 415, 3552–3560. doi:10.1111/j.1365-2966.2011.18970.x.

Howell, K.C., 1984. Three-dimensional periodic halo orbits. Celest. Mech. 32, 53–71. doi:10.1007/BF01358403.

Kirk, D.E., 2004. Optimal control theory: an introduction. Dover, Mineola, New York.

Lou, Z., Zhang, K., Wang, Y., Gao, Q., 2016. Active disturbance rejection station-keeping control for solar-sail libration-point orbits. J. Guid. Control Dyn. 39, 1917–1921. doi:10.2514/1.G001722.

McInnes, A., 2000. Strategies for solar sail mission design in the circular restricted three-body problem. M.S.E. Thesis, Purdue University .

McInnes, C.R., 1999. Solar sailing: technology, dynamics and mission applications. Springer and Praxis, Chichester, UK.

Mengali, G., Quarta, A.A., 2016. Heliocentric trajectory analysis of sun-pointing smart dust with electrochromic control. Adv. Space Res. 57, 991–1001. doi:10.1016/j.asr.2015.12.017.

Mengali, G., Quarta, A.A., Denti, E., 2018. Relative motion of sun-pointing smart dust in circular heliocentric orbits. J. Guid. Control Dyn. 41, 1015–1020. doi:10.2514/1.G003088.

Mu, J., Gong, S., Li, J., 2015. Coupled control of reflectivity modulated solar sail for geosail formation flying. J. Guid. Control Dyn. 38, 740–751. doi:10.2514/1.G000117.

Niccolai, L., Bassetto, M., Quarta, A.A., Mengali, G., 2019. A review of smart dust architecture, dynamics, and mission applications. Prog. Aerosp. Sci. 106, 1–14. doi:10.1016/j.paerosci.2019.01.003.

Richardson, D.L., 1980a. Analytic construction of periodic orbits about the collinear points. Celest. Mech. 22, 241–253. doi:10.1007/BF01229511.

Richardson, D.L., 1980b. Halo orbit formulation for the isee-3 mission. J. Guid. Control 3, 543–548. doi:10.2514/3.56033.

Richardson, D.L., 1980c. A note on a lagrangian formulation for motion about the collinear points. Celest. Mech. 22, 231–236. doi:10.1007/BF01229509.

Shirobokov, M., Trofimov, S., Ovchinnikov, M., 2017. Survey of station-keeping techniques for libration point orbits. J. Guid. Control Dyn. 40, 1085–1105. doi:10.2514/1.G001850.

Szebehely, V., 1967. Theory of orbits: the restricted problem of three bodies. Academic Press, New York and London. pp. 587–595.

Verrier, P., Waters, T., Sieber, J., 2014. Evolution of the [formula] halo family in the radial solar sail circular restricted three-body problem. Celest. Mech. Dyn. Astr. 120, 373–400. doi:10.1007/s10569-014-9575-2.

Waters, T.J., McInnes, C.R., 2007. Periodic orbits above the ecliptic in the solar-sail restricted three-body problem. J. Guid. Control Dyn. 30, 687–693. doi:10.2514/1.26232.

Yuan, J., Gao, C., Zhang, J., 2018. Periodic orbits of solar sail equipped with reflectance control device in earth–moon system. Astrophys. Space Sci. 363, 23. doi:10.1007/s10509-017-3223-8.

Zeng, X., Vulpetti, G., Circi, C., 2019. Solar sail h-reversal trajectory: A review of its advances and applications. Astrodyn. 3, 1–15. doi:10.1007/s42064-018-0032-y.